

# Structural signature and transition dynamics of $\text{Sb}_2\text{Te}_3$ melt upon fast cooling

Y. R. Guo,<sup>1</sup> F. Dong,<sup>1</sup> C. Qiao,<sup>1</sup> J. J. Wang,<sup>1</sup> S. Y. Wang,<sup>1,2,\*</sup> Ming. Xu,<sup>3,\*</sup> Y. X. Zheng,<sup>1</sup> R. J. Zhang,<sup>1</sup> L. Y. Chen,<sup>1</sup> C. Z. Wang,<sup>4</sup> and K. M. Ho<sup>4</sup>

<sup>1</sup>*Shanghai Ultra-Precision Optical Manufacturing Engineering Center and Department of Optical Science and Engineering, Fudan University, Shanghai, 200433, China*

<sup>2</sup>*Key Laboratory for Information Science of Electromagnetic Waves (MoE), Shanghai 200433, China*

<sup>3</sup>*School of Optical & Electronic Information, Huazhong University of Science & Technology, Wuhan, 430074, China*

<sup>4</sup>*Ames Laboratory, U. S. Department of Energy and Department of Physics and Astronomy, Iowa State University, Ames, Iowa 50011, USA*

## Corresponding Authors

\*Email: [songyouwang@fudan.edu.cn](mailto:songyouwang@fudan.edu.cn) ; [mxu@hust.edu.cn](mailto:mxu@hust.edu.cn)

## ABSTRACT

The crystalline  $\text{Sb}_2\text{Te}_3$  is widely studied due to its important applications in memory materials and topological insulators. The liquid and amorphous structures of this compound as well as the dynamics upon quenching, however, is yet to be fully understood. In this work, we have systematically studied the dynamical properties and local structure of  $\text{Sb}_2\text{Te}_3$  at different temperatures by ab initio molecular dynamics simulations. The calculated structure factors agree well with the experimental results. The atomic number density and mean-squared displacement as a function of temperature clearly indicate three states as the temperature decreases, namely, melt, undercooled liquid and glass state, respectively. By analyzing the chemical environments and bond-angle distribution functions, we demonstrate that the most probable short-range motifs in  $\text{Sb}_2\text{Te}_3$  system are

defective octahedrons, and they are connected with each other via four-fold rings. This interesting structural feature may be responsible for the large fragility and easy phase transition upon glass forming that is applied in memory devices.

**Keywords:** first principles, liquid materials, local structure, Phase-change materials.

## I. INTRODUCTION

Phase-change materials (PCMs) are widely applied to large capacity rewritable optical and electronic data storage, such as rewritable Digital Video Discs (DVDs) and phase-change random access memories (PCRAM), which take advantage of the reversibly transformation between the amorphous and crystalline phases upon heating or electric current.<sup>1-3</sup> The prototypical PCM for this purpose is Ge-Sb-Te (GST), located on the pseudo-binary line between GeTe and Sb<sub>2</sub>Te<sub>3</sub> compounds.<sup>4,5</sup> In spite of extensive studies of this material over the decades,<sup>6-8</sup> many of its structural and electronic properties as well as the phase change dynamics remain to be fully understood.

As an important prototypical phase change material, a lot of theoretical and experimental researches have been devoted to crystalline Sb<sub>2</sub>Te<sub>3</sub>. Crystalline Sb<sub>2</sub>Te<sub>3</sub> is also a new class of three-dimensional topological insulators with layered rhombohedral crystal structure.<sup>9-11</sup> Under strong spin-orbit coupling, the topological insulator has a lot of unique quantum properties, which has been attracting a lot of attentions in recent years.<sup>12, 13</sup> In contrast to the crystalline phase, there are fewer reports about the liquid and amorphous states of Sb<sub>2</sub>Te<sub>3</sub> by theoretical studies. Previous work have studied local geometrical environment, electronic and vibrational properties of liquid and amorphous Sb<sub>2</sub>Te<sub>3</sub>,<sup>14</sup> however, the understanding of the temperature dependence of structural transition and dynamical properties in liquid and amorphous states of Sb<sub>2</sub>Te<sub>3</sub> remains insufficient, and thus is of great interest to be further investigated. The liquid and amorphous Sb<sub>2</sub>Te<sub>3</sub> has many fascinating properties for the applications in memory devices, e.g., the crystallization speed of Sb-Te binary phase-change materials is extremely fast, and when doped with other elements such as Ge, Al,<sup>15</sup> In,<sup>16, 17</sup> Ag,<sup>18</sup> its crystallization temperature becomes tunable as well as the stability is enhanced, which is balanced for low-power consumption and long data retention.<sup>19</sup> In the latest research, alloying with Sc not only improves its stability at room temperature, but also significantly enhances the crystallization speed at elevated temperatures by one order of magnitude via

stabilizing the fourfold rings in  $\text{Sb}_2\text{Te}_3$ .<sup>20</sup>

In fundamental materials science, when the melt is cooled rapidly below the melting temperature, it turns into a “undercooled liquid” state without instant crystallization.<sup>21-23</sup> If the temperature continues to decrease and the cooling rate is fast enough, the undercooled liquid can be “frozen” into a glass state. To date, a complete understanding of the liquid-amorphous phase evolution of  $\text{Sb}_2\text{Te}_3$  as well as the structural and dynamical properties of liquid state at the atomic level is still lacking. As the micro-structure of materials majorly impacts their properties, the quantitative exploring of the relationships between macroscopic property and micro-structure is the primary researching goal of computational materials science. Thus, it is important to systematically explore the structural signature of the glassy state, undercooled and liquid state of materials. Understanding the temperature dependence of the chemical environment, atomic structure and bonding mechanism sheds light on the characteristics of  $\text{Sb}_2\text{Te}_3$  and other PCMs.

In this work, *ab initio* molecular dynamics (AIMD) simulations were performed to study the local atomic ordering as well as the kinetic properties in the liquid and amorphous phases of  $\text{Sb}_2\text{Te}_3$ . The simulation results in our work were compared with available experimental data and previous theoretical works, showing good agreement. In addition, the short- and medium-range orders (SRO and MRO) in the undercooled and glass states of  $\text{Sb}_2\text{Te}_3$  were explored. We show that in a- $\text{Sb}_2\text{Te}_3$ , Sb atoms prefer to maintain the defective octahedral configuration and those octahedral clusters connect with each other via fourfold rings. The results of these theoretical simulations will contribute to understanding the phase-change mechanism of PCMs.

## II. METHODS

The AIMD simulations of the  $\text{Sb}_2\text{Te}_3$  were carried out using the Vienna *ab initio* simulation package (VASP) code based on the density functional theory,<sup>24, 25</sup> with the projector-augmented wave (PAW) method<sup>26, 27</sup> and the Perdew-Burke-Ernzerhof form of generalized gradient approximation pseudopotentials (GGA-PBE).<sup>28</sup> The

simulations were performed using a NVT (canonical) ensemble and the temperature is controlled by Nose-Hoover thermostat.<sup>29, 30</sup> Only the  $\Gamma$  point was applied in the Brillouin zone.

The starting configuration for the AIMD simulation was a cubic supercell consisting of 80 Sb and 120 Te atoms with random distribution. Then, the temperature was set to 2000 K (the melting point of  $\text{Sb}_2\text{Te}_3$  is 890 K<sup>31</sup>) in order to eliminate the memory effect on the initial configuration, and the liquid state was stabilized at 1223 K. Periodic boundary conditions were used in the simulation. The  $\text{Sb}_2\text{Te}_3$  was then cooling down from 1223 K to 300 K, with a constant cooling rate of 33.3 K/ps and the time step of 3 fs in this work. At each temperature, the atomic number density of the system was adjusted to ensure the internal pressure of the system close to zero (within  $0.0\pm 0.5$  kB) by varying the size of the simulation box. The system was stabilized at the interval of 50 K for 6000 steps using a NVT (constant-number of particles, constant-temperature, constant-volume) ensemble during the cooling. The last 4000 trajectories at each temperature were collected for the analysis of the local structure and kinetic properties. By using above MD trajectories, the pair correlations functions, bond-angle distribution, ring statistics as well as atomistic cluster alignment (ACA) method<sup>32</sup> were employed to study the local order.

The ACA method includes collective alignment and one-on-one cluster-template alignment. For the collective alignment part, a simulated annealing scheme implemented with MD simulation is performed. Two interatomic potentials are used in the MD simulated annealing, while one is a modified Lenard-Jones-type attractive potential which describes the attractive interaction between the atoms in different local clusters, and the other is a strong harmonic potential which describes character between atom pairs within the same cluster to keep the structure quasi-rigid during the alignment process. The randomly selected clusters in the system are translated and rigidly rotated relatively to each other to minimize the overall mean-square distances among different clusters. Then collective alignment results for atomic density are obtained in three-dimensional space by using the Gaussian smearing scheme. For

one-on-one cluster-template alignment, the given templates are used to perform alignment with selected local clusters in the system under the potentials. The obtained structural similarity with the given templates classifies the clusters in the system into different types of SRO.

### III. RESULTS AND DISCUSSION

The atomic number density ( $\rho$ ) of the simulated  $\text{Sb}_2\text{Te}_3$  at different temperatures is shown in Fig. 1. Obviously, the curve has three different sections, and the two inflexion points are 1023 K and 423 K respectively. The experimental melting temperature of  $\text{Sb}_2\text{Te}_3$  is 890 K<sup>31</sup>, so the temperatures above 1023 K should be classified as liquid state. When  $\text{Sb}_2\text{Te}_3$  is cooled down rapidly from the liquid, the compound will first turn into the undercooled liquid and then amorphous state if it fails to crystallize. The material between the turning temperatures (1023 K-423 K) can be regarded as undercooled liquid state. Accordingly, the temperatures below 423 K should be glass state.

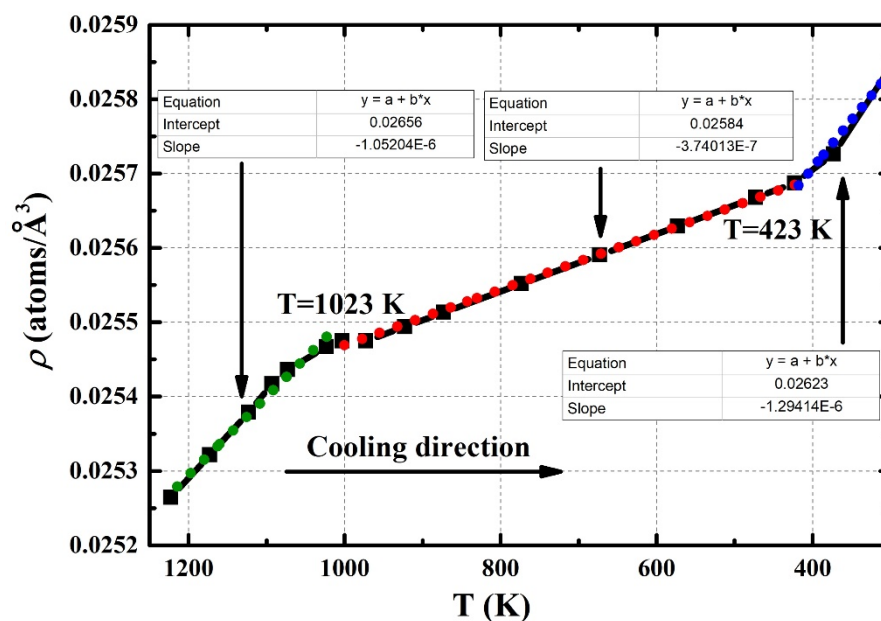


Fig. 1. The atomic number density of  $\text{Sb}_2\text{Te}_3$  during quenching is simulated in black curve. The three different slopes are fitted in three colors of the straight line: green

dots represent liquid state and red dots cover undercooled liquid state, and blue dots stand for glass state. The fitting slope of green dots, red dots and blue dots are  $-1.05\text{E-}6$ ,  $-3.74\text{E-}7$ , and  $-1.29\text{E-}6$ , respectively.

Mean-squared displacement (MSD) is an important dynamical property parameter to characterize atomic mobility. The MSD as a function of time is defined as follows:

$$\langle R_{\alpha}^2(t) \rangle = \frac{1}{N_{\alpha}} \langle \sum_{i=1}^{N_{\alpha}} |R_{i\alpha}(t + \tau) - R_{i\alpha}(\tau)|^2 \rangle \quad (1)$$

where  $N_{\alpha}$  is the number of  $\alpha$  atoms,  $R_{i\alpha}$  are the coordinates of atom  $i$ , and  $\tau$  is the arbitrary origin of time. The self-diffusion coefficient  $D$  can be obtained from the time-dependent MSD through the Einstein relation,

$$6Dt = \lim_{t \rightarrow \infty} \langle R_{\alpha}^2(t) \rangle \quad (2)$$

As shown in the left of Fig. 2, the calculated MSD at the undercooled liquid and liquid state exhibit a nearly linear behavior. Self-diffusion coefficients in the undercooled liquid and liquid state (temperature above 573 K) are shown in Fig. 2. Calculated self-diffusion coefficients show an approximately linear increase with temperature, implying that the mobility of atoms in the liquid are enhanced gradually with temperature. The self-diffusion coefficient is usually described by the Arrhenius equation:

$$D = D_0 \exp\left(-\frac{E_{\alpha}}{k_B T}\right) \quad (3)$$

where  $E_{\alpha}$  is denoted as the activation energy and  $D_0$  as the pre-exponential factor. The relation between  $\ln(D)$  and  $1/T$  is shown in the right-hand panels of Fig. 2, and activation energy  $E_{\alpha}$  is evaluated from the slope as 24.35, 23.59, 24.81 kJ/mol for the liquid, Sb and Te, respectively. The pre-exponential factor  $D_0$  of Sb and Te is  $1.006 \times 10^{-7}$  and  $1.258 \times 10^{-7}$  m<sup>2</sup>/s, respectively. The mobility of two constituents are almost identical, while the self-diffusion coefficient of Te is a little larger than that of Sb, showing Te atoms diffuse slightly faster than Sb atoms, which agrees with experimental results.<sup>33</sup>

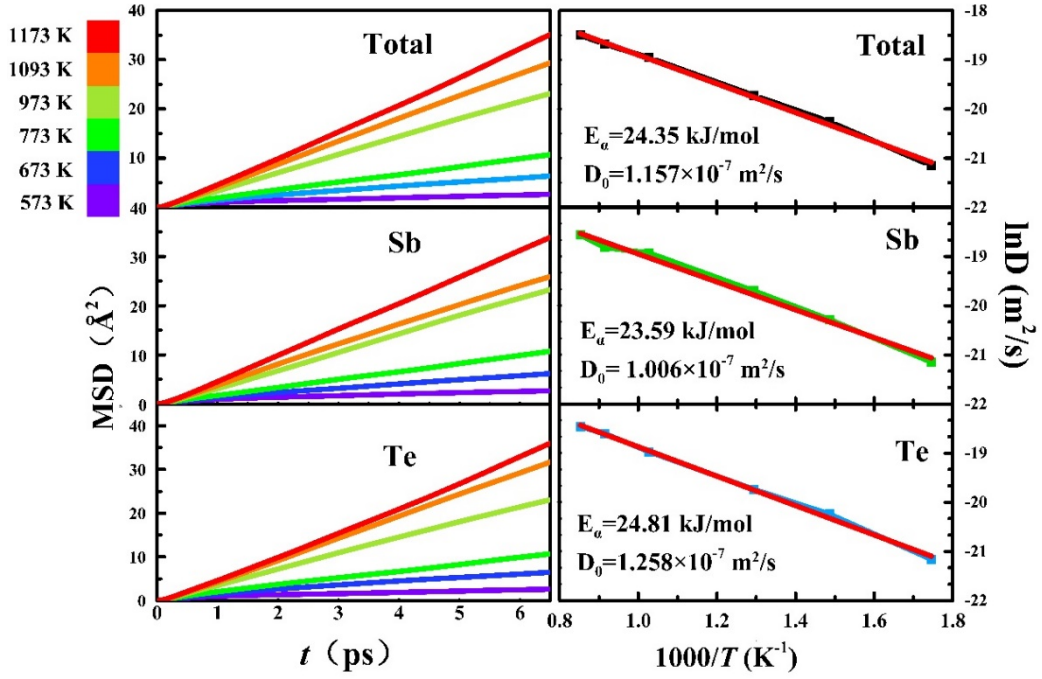


Fig. 2. The MSD and self-diffusion coefficient  $D$  of  $\text{Sb}_2\text{Te}_3$  at different temperatures.

The experimental structure factors  $S(q)$  for liquid  $\text{Sb}_2\text{Te}_3$  measured by neutron diffraction at 1093 K, 1003 K, 923 K<sup>34</sup> are compared with the calculated structure factors in Fig. 3. The simulated  $S(q)$  for  $\text{Sb}_2\text{Te}_3$  at three temperatures is in good agreement with experimental results.

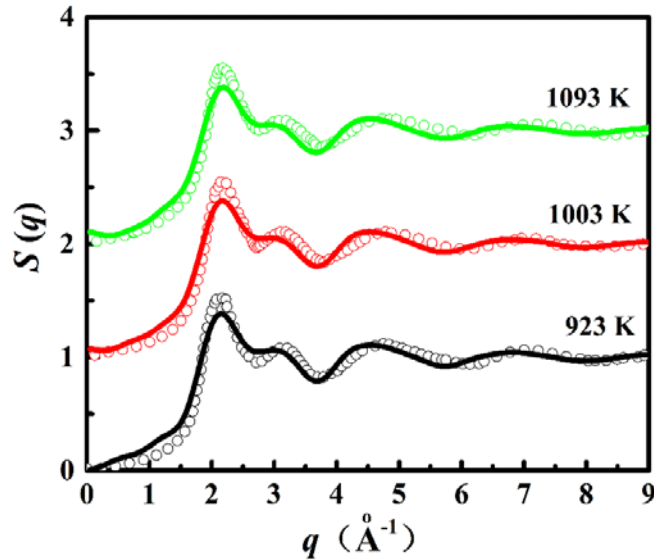


Fig. 3. Total structure factor  $S(q)$  of  $\text{Sb}_2\text{Te}_3$  at 1093 K, 1003 K, 923 K. Solid lines and open circles represent the simulation data and the neutron diffraction experimental data, respectively.

There are many methods to determine coordination numbers (CNs), such as

crystal orbital overlap population (COOP),<sup>35, 36</sup> electron localization function (ELF) analysis,<sup>37</sup> etc., and here we use an “uniform cutoff” to determine CNs. This cutoff value is close to the first minimum in the total pair-correlation function. The calculated total and partial CNs are presented in Fig. 4. The CNs of Sb-Te and Te-Sb obviously increase with the decrease of temperature, revealing the closer packing between Sb and Te atoms. It is found that a fair amount of homopolar bonds exist in liquid state. Sb atoms are mostly around three and four-fold coordinated while Te atoms are mostly around two and three-fold. Comparing with previous theoretical works,<sup>14, 19</sup> average CNs of Sb and Te atoms are a little smaller due to the smaller cutoff distance used in our works.

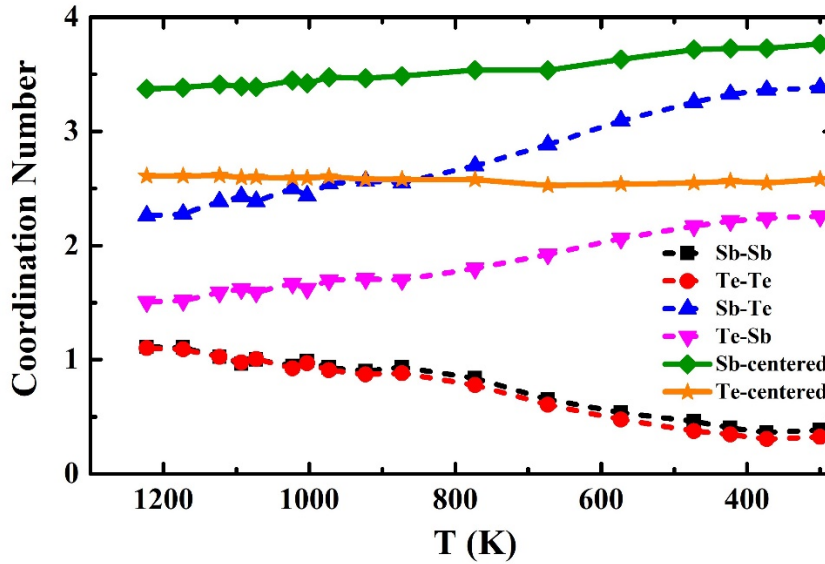


Fig. 4. Coordination number of  $\text{Sb}_2\text{Te}_3$  at different temperatures. The solid lines labelled as Sb-centered and Te-centered represent the total CNs of Sb and Te atoms, respectively. The dashed lines labelled as A-B are partial CNs, which indicate that A is the central atom and B is the coordination atom. The uniform cutoff distance is 3.3 Å.

There is no universal criterion for the cutoff distance and the obtained CNs are always influenced by this choice.<sup>38, 39</sup> Besides the “uniform cutoff” distances above, we calculated the CNs with a different partial cutoff (Sb-Sb 3.26 Å, Sb-Te 3.85 Å, Te-Te 3.16 Å, the first minimum of the corresponding pair-correlation functions), as

listed in table II. The uniform cutoff enables us to determine the nearest bonded neighbors, while partial cutoff could reveal the local structure in a larger scale (e.g., some unbonded neighbors interacted with van der Waals force are included). Using this new cutoff, the total CNs become 5.42 and 3.43 for Sb and Te at 300 K, which are similar to the ideal octahedral coordination of 6 and 4. Five and sixfold coordinated for Sb atoms accounts are 36.9% and 47.9% respectively, and the most common configuration is Sb-Te<sub>6</sub> (CN=6), amounting 38.9% of the Sb-centered atoms. Meanwhile the proportion of three and fourfold coordinated for Te atoms are 41.6% and 33.0% respectively, and the most dominant one is Te-Sb<sub>3</sub> (CN=3), the percentage contents up to 31.5%.

Table II. Average CNs of Sb and Te atoms using a uniform cutoff distance at 300 K. The value in parenthesis is the CNs calculated from partial cutoff distance.

	With Sb	With Te	Total
Sb	0.38 (0.37)	3.38 (5.05)	3.77 (5.42)
Te	2.26 (3.36)	0.33 (0.27)	2.58 (3.63)

The chemical SRO describes the interactions between different atomic species, which determines the structural and thermodynamic properties in binary alloys. It can be evaluated effectively by the Warren-Cowley chemical SRO parameter<sup>40</sup>  $\alpha_{ij}$  in disordered systems. The equation of  $\alpha_{ij}$  is illustrated as follows:

$$\alpha_{ij} = 1 - N_{ij}/c_j N_{tot} \quad (4)$$

where  $N_{ij}$  is the CN of  $j$  type atoms around  $i$  type atoms and  $N_{tot}$  are the total CNs around  $i$  type atoms and  $c_j$  is the concentration of the  $j$  partial. The calculated Warren-Cowley chemical SRO parameters of Sb<sub>2</sub>Te<sub>3</sub> at different temperatures are displayed in Fig. 5. The negative values of  $\alpha_{Sb-Te}$  indicate a tendency to form attractive Sb-Te bonds, while the positive values of  $\alpha_{Te-Te}$  and  $\alpha_{Sb-Sb}$  suggest that the formation of Te-Te or Sb-Sb bonds are not favorable. Hence, there is an affinity interaction between Sb and Te atoms and a relatively “repulsive” interaction in Te-Te

and Sb-Sb pairs which are not as preferable as heteropolar Sb-Te bonds. Interestingly, as temperature decreases, the bonding energy between Sb and Te atoms becomes stronger, while the homopolar bonds are less likely to form. This indicates the system become more ordered upon cooling, which is consistent with the previous results of CN.

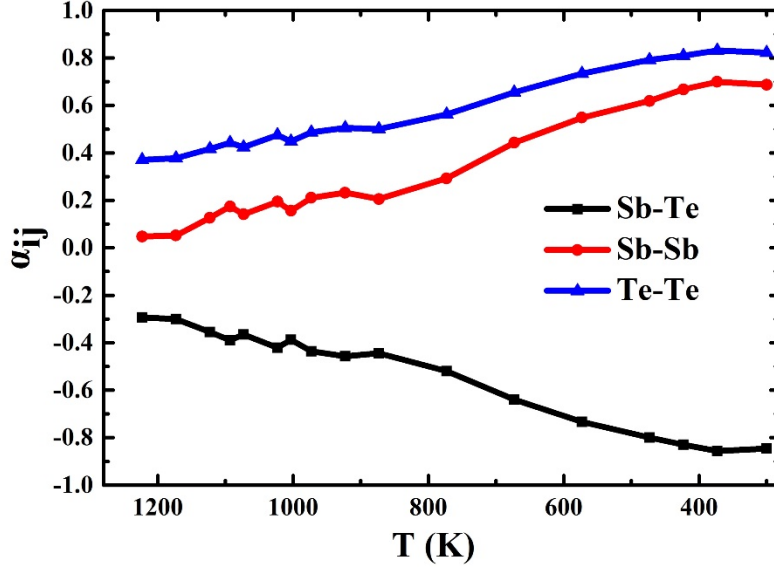


Fig. 5. The Warren-Cowley chemical SRO parameter of  $\text{Sb}_2\text{Te}_3$  at different temperatures.

To further explore the information about chemical and topological orders in  $\text{Sb}_2\text{Te}_3$ , we calculated the bond-angle distribution functions (Fig. 6) at different temperatures. Bond-angle distribution functions  $g_3(\theta)$  represent the distribution of bond-angle between a specific atom and its two neighboring atoms within a cutoff distance. We divided six partial bond-angle distribution functions into two groups: aSb-centered group as plotted in Fig. 6(a)-(c), and a Te-centered group as plotted in Fig. 6(d)-(f), respectively. It can be seen from Fig. 6, the main peak in the angle distribution function is around  $90^\circ$  for Sb-Te-Sb and Te-Sb-Te which is more prominent among all the partial bond-angle distribution functions. Remarkably, there is a small peak located at about  $167^\circ$  for Te-Sb-Te because the main bonding angle around  $90^\circ$  and the lower peak angle close to  $180^\circ$  are the characteristic of the

defective octahedral geometry. What's more, the main peak in the angle distribution function becomes sharper as the temperature decrease, which can be attributed to the increase of defective octahedral-like geometries in  $\text{Sb}_2\text{Te}_3$  as the temperature is lowered. The angle distribution functions of Sb-Sb-Te and Sb-Te-Te are similar with two main peaks locate at about  $55^\circ$  and  $90^\circ$  respectively. However, the peak intensities of Sb-Sb-Sb and Te-Te-Te are much lower than that in Sb-Te-Sb and Te-Sb-Te, indicating that the bonding mode of Sb (Te) atom bond with another two neighboring Sb (Te) atoms is relatively fewer.

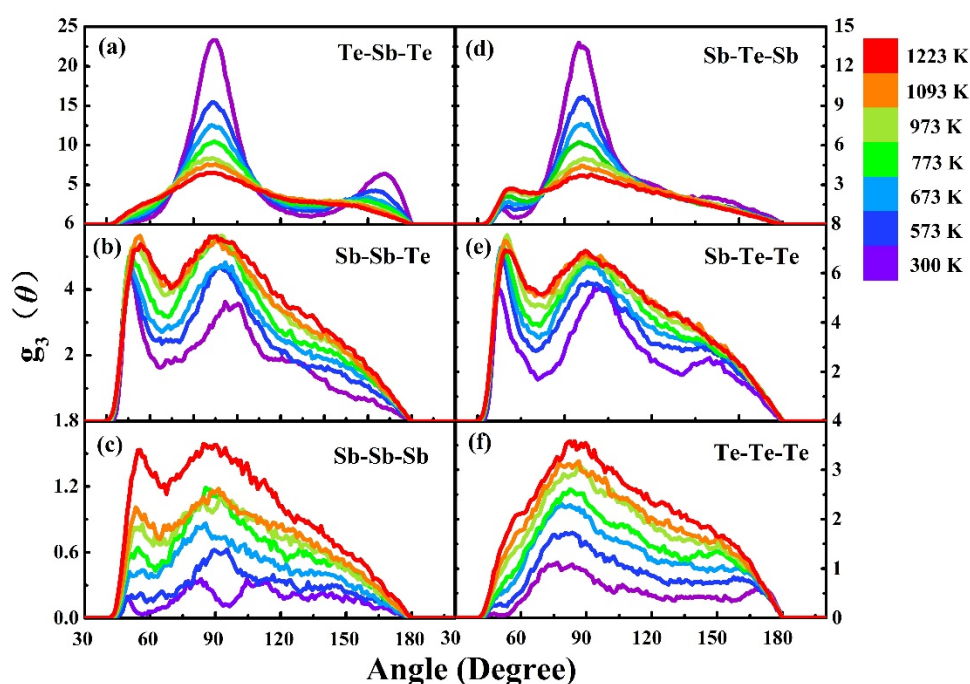


Fig. 6. The calculated partial bond-angle distribution functions of  $\text{Sb}_2\text{Te}_3$  at different temperatures.

To better understand the local structure in  $\text{Sb}_2\text{Te}_3$ , we carried out analysis using the atomistic cluster alignment (ACA) method<sup>32</sup> proposed in recent years. ACA method consists of two parts: collective alignment and one-on-one cluster-template alignment. In this study, 3000 clusters for each type of central atoms were randomly selected from the MD simulation trajectories at each temperature of 300 K, 673 K and 1093 K respectively. Each cluster is composed of 7 nearest neighboring atoms and all those clusters are overlapped to the central atoms. Then, the collective alignment is

performed by applying rigid rotation as well as translational operations to the clusters until the overall mean-square distance among all the clusters is minimized. After the collective alignment, we obtain three-dimensional atomic density distributions smoothed with Gaussian smearing. The collective alignments of  $\text{Sb}_2\text{Te}_3$  at 300 K, 673 K and 1093 K are plotted in Fig. 7. Overall, the defective octahedral-like geometry stands out in  $\text{Sb}_2\text{Te}_3$ . This is reminiscent of the crystalline  $\text{Sb}_2\text{Te}_3$ , which contains many octahedral patterns as well. The Sb-centered clusters show the pattern of octahedral order in both glass state  $\text{Sb}_2\text{Te}_3$  (300 K) and undercooled liquid  $\text{Sb}_2\text{Te}_3$  (673 K). However, Te-centered clusters exhibit more complex octahedral patterns, and the SRO become less well-defined when the temperature rises above 673K. Therefore, the octahedral-like geometry for Sb-centered clusters are more stable than that of Te-centered clusters in  $\text{Sb}_2\text{Te}_3$ . Obviously, the whole system is in a state of disorder at 1093 K, showing less well-defined SRO structure in liquid- $\text{Sb}_2\text{Te}_3$ .

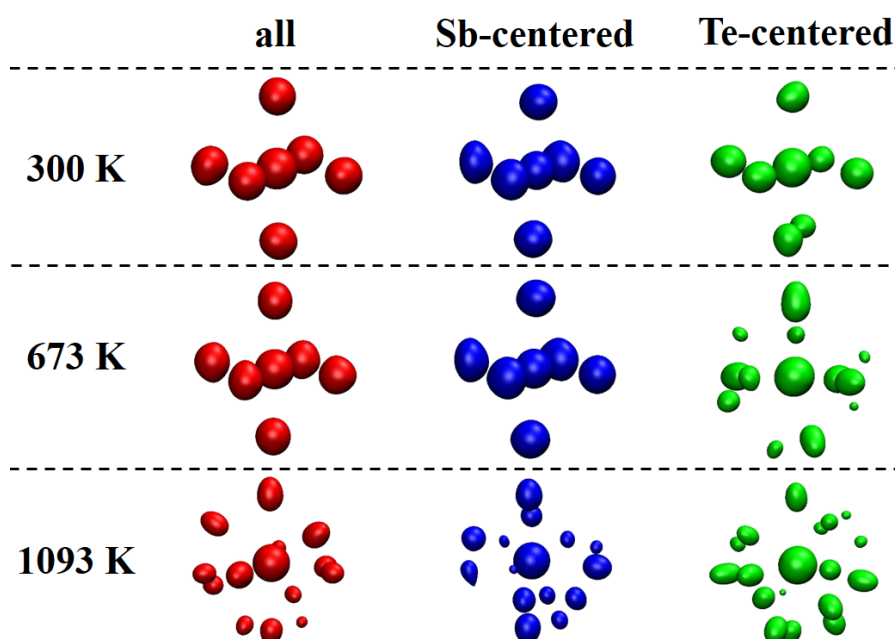


Fig. 7. The collective alignments of  $\text{Sb}_2\text{Te}_3$  at 300 K, 673 K and 1093 K shows interesting evolution of SRO. Clusters in left is the overall (red) local motif. Clusters in middle and in right stand for the Sb (blue) and Te (green) centered ones. The isovalue is set to be  $0.15 \text{ \AA}^{-3}$ .

By using one-on-one cluster-template alignment scheme of ACA, we identify the

distorted Sb-centered octahedral clusters in a snapshot at 300 K and study the spatial distribution and connections of these clusters in the glass sample. The template is chosen as the distorted Sb-centered octahedral cluster made up of 7 atoms obtained from the collective alignment. Each Sb-centered cluster extract from the glass sample at 300 K is aligned against this template to determine its structural similarity with the template. If the alignment score is less than 0.2, we assign the cluster to be a Sb-centered octahedral cluster. The population of clusters in the system according to their structural similarity with the given template are 28.8%, 7.9% and 1.9% for 300 K, 673 K and 1093 K, respectively. The spatial distribution of these clusters in the glass sample is plotted as shown in Fig. 8, which shows the network of distorted Sb-centered octahedral clusters in the  $\text{Sb}_2\text{Te}_3$  glass sample at 300 K when Te-Te distance cutoff is set to be 3.3 Å and 5.5 Å respectively. The green spheres represent the center atoms (Sb atoms), and the purple ones represent the neighbor atoms (Te atoms). In Fig. 8(a), the cutoff value is 3.3 Å, which is the nearest neighbor of Te-Te atoms. We can see that only a few clusters are connected with such a Te-Te cutoff distance. However, if we take the next nearest neighbor of Te-Te atoms as cutoff value (5.5 Å) the distorted Sb-centered octahedral are all connected with each other and form a network as displayed in Fig. 8(b). Thus, it can be inferred that there are stronger interactions of the next neighbors between Te atoms. Moreover, almost all six atoms of the nearest neighbor atoms are Te atoms for those Sb-centered clusters, which is consistent with the CN results that the most common configuration is Sb-Te<sub>6</sub> in the glass of  $\text{Sb}_2\text{Te}_3$ .

Medium-range order (MRO) is complex yet important structural information in the networks of amorphous systems which can also be analyzed by ring statistics. Using the RINGS code,<sup>41</sup> we compute the primitive rings statistics in crystalline  $\text{Sb}_2\text{Te}_3$  and in the  $\text{Sb}_2\text{Te}_3$  glass sample which was used to perform the one-on-one cluster-template alignment above. The results are shown in Fig. 9. In both c- $\text{Sb}_2\text{Te}_3$  and a- $\text{Sb}_2\text{Te}_3$ , four-fold rings are the most prevalent ones, indicating that there is structural similarity between crystalline and amorphous  $\text{Sb}_2\text{Te}_3$ . Analogously, it has

been reported that in amorphous GST compounds, four-fold rings are the building blocks of the metastable rocksalt structure and can be regarded as crystalline seeds in the amorphous phase.<sup>42-44</sup> Thus, four-fold rings are the basic structural elements for fast phase transition in PCMs.<sup>20</sup> Meanwhile, a-Sb<sub>2</sub>Te<sub>3</sub> exhibits some fraction of other even-fold rings owing to the formation of homopolar bonds which is the same as in GeTe.<sup>45</sup> On the other hand, the fraction of large rings such as sixteen-, fourteen- and twelve-fold rings also take up a great portion, indicating a somehow more open structure.

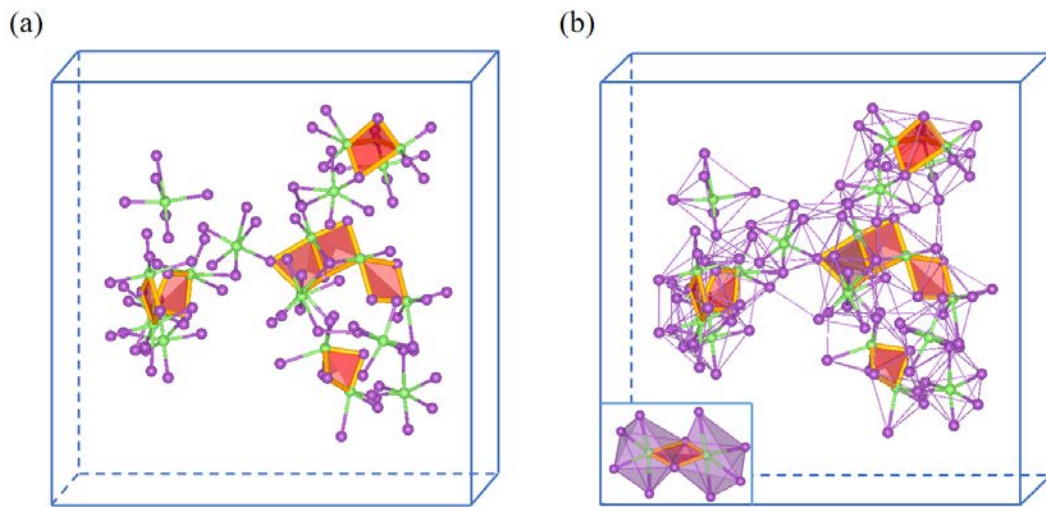


Fig. 8. The comparison in glass state Sb<sub>2</sub>Te<sub>3</sub> of two different bonding cutoff distances for the snapshots in boxes. (a) 3.3 Å is the nearest neighbor of Te-Te atoms, and (b) 5.5 Å is the next nearest neighbor of Te-Te atoms. The green atoms represent Sb atoms. The purple atoms represent Te atoms. The connected four-fold rings for glass state Sb<sub>2</sub>Te<sub>3</sub> highlight in red polyhedron with gold bonds. The inset shows the defective octahedrons connected with each other via four-fold rings.

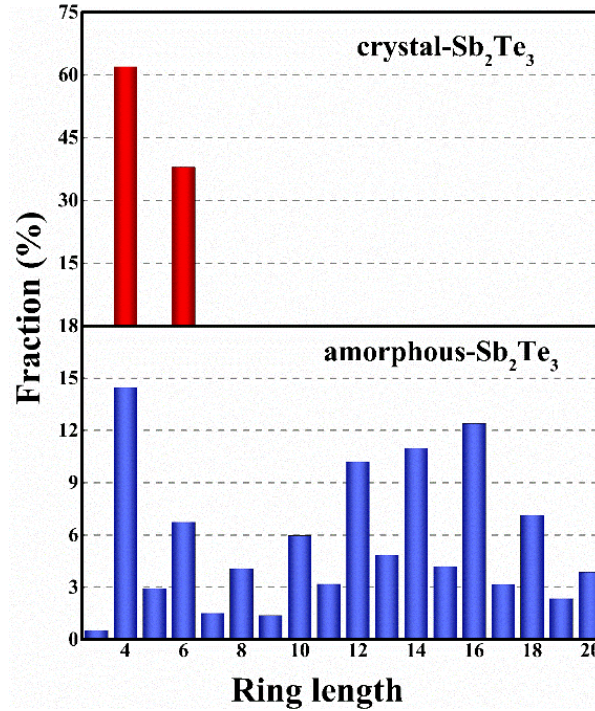


Fig. 9. Ring distribution fraction of c-Sb<sub>2</sub>Te<sub>3</sub> and a-Sb<sub>2</sub>Te<sub>3</sub>.

In the Sb-centered octahedral cluster network shown in Fig. 8, the most abundant rings are also the four-fold rings with alternating atoms of Sb (A) and Te (B) in a “ABAB square” occupying about 76.2% of the proportion of the four-fold rings. These Sb-centered defective octahedrons connect with each other via four-fold rings, and thus a close link of the four-fold ring and defective octahedrons in amorphous solid systems has been revealed.

#### IV. CONCLUSIONS

In conclusion, the local structures of Sb<sub>2</sub>Te<sub>3</sub> in amorphous and liquid states are studied by ab initio molecular dynamics simulations. Sb<sub>2</sub>Te<sub>3</sub> has undergone three states according to atomic number density and MSD upon cooling: melt, undercooled liquid and glass, respectively. The calculated structural factors are in good agreement with the experiments. CN results and chemical SRO parameters indicate that Sb-Te bonds are more favorable than Te-Te and Sb-Sb bonds. In addition, the ACA method was employed to obtain a 3D description of the average structure ordering in the system and a consistent result was revealed. When the Te-Te cutoff distance is

selected to be 5.5 Å which is the same as the second nearest neighbors, it is found that those defective octahedrons connect with each other via fourfold rings. Such a large fraction of fourfold rings and some homopolar bonds are presented in a-Sb<sub>2</sub>Te<sub>3</sub>, similar to those appeared in a-GST. This work provides useful insight into the local structural characteristics and phase change mechanisms of a-Sb<sub>2</sub>Te<sub>3</sub>, and our simulations of Sb<sub>2</sub>Te<sub>3</sub> during quenching enrich the knowledge of the Sb-Te alloys in the liquid and amorphous states for the applications of memory materials and topological insulators.

## **ACKNOWLEDGMENTS**

Work at Fudan University was supported by the NSF of China (Grant No. 11374055 and 61427815) and the Fudan High-end computing center. M.X. acknowledges National Key R&D Plan of China (Grant No. 2017YFB0701700 “Materials Genome Engineering”) and the NSF of China (Grant No. 51772113). Work at Ames Laboratory was supported by the US Department of Energy, Basic Energy Sciences, and Division of Materials Science and Engineering, including a grant of computer time at the National Energy Research Scientific Computing Centre (NERSC) in Berkeley, CA under. Ames Laboratory is operated for the U.S. DOE by Iowa State University under contract # DE-AC02-07CH11358.

## **Author contributions**

Y. R. Guo performed the theoretical calculations. Y. R. Guo, F. Dong, C. Qiao, J. J. Wang, S. Y. Wang, M. Xu, C. Z. Wang and K. M. Ho contributed to the data analyses; Y. X. Zheng, R. J. Zhang and L. Y. Chen discussed and interpreted the results. Y. R. Guo, M. Xu, C. Z. Wang, and S. Y. Wang wrote the paper.

## REFERENCES

1. E. Kuramochi and M. Notomi, *Nat. Photonics*, 2015, **9**, 712-714.
2. D. Loke, T. H. Lee, W. J. Wang, L. P. Shi, R. Zhao, Y. C. Yeo, T. C. Chong and S. R. Elliott, *Science*, 2012, **336**, 1566-1569.
3. M Wuttig and N. Yamada, *Nat. Mater*, 2007, **6**, 824-832.
4. N. Yamada, E. Ohno, N. Akahira, N. Nishiuchi, K. Nagata and M. Takao, *Jpn. J. Appl. Phys.*, 1987, **26**, 61-66.
5. R. E. Simpson, M. Krbal, P. Fons, A. V. Kolobov, J. Tominaga, T. Uruga and H. Tanida, *Nano Lett.*, 2010, **10**, 414-419.
6. M. Schumacher, H. Weber, P. Jovari, Y. Tsuchiya, T. G. Youngs, I. Kaban and R. Mazzarello, *Sci Rep*, 2016, **6**, 27434.
7. S. Kumar, D. Singh, S. Sandhu and R. Thangaraj, *Phys. Status Solidi (a)*, 2012, **209**, 2014-2019.
8. J. Takeda, W. Oba, Y. Minami, T. Saiki and I. Katayama, *Appl. Phys. Lett.*, 2014, **104**, 261903.
9. W. Zhang, R. Yu, H.-J. Zhang, X. Dai and Z. Fang, *New J. Phys.*, 2010, **12**, 065013.
10. G. C. Sosso, S. Caravati and M. Bernasconi, *J. Phys. Condens. Matter* 2009, **21**, 095410.
11. B. Sa, J. Zhou, Z. Sun, J. Tominaga and R. Ahuja, *Phys. Rev. Lett.*, 2012, **109**, 096802.
12. Q. Lu, H.-Y. Zhang, Y. Cheng, X.-R. Chen and G.-F. Ji, *Chin. Phys. B*, 2016, **25**, 026401.
13. I. A. Nechaev, I. Aguilera, V. De Renzi, A. di Bona, A. Lodi Rizzini, A. M. Mio, G. Nicotra, A. Politano, S. Scalese, Z. S. Aliev, M. B. Babanly, C. Friedrich, S. Blügel and E. V. Chulkov, *Phys. Rev. B*, 2015, **91**, 245123.
14. S. Caravati, M. Bernasconi and M. Parrinello, *Phys. Rev. B*, 2010, **81**, 014201.
15. L. Zhang, S. Song, W. Xi, L. Li, Y. He, H. Lin and Z. Song, *J. Phys. Chem. Solids.*, 2015, **83**, 52-57.
16. J. H. Los, T. D. Kühne, S. Gabardi and M. Bernasconi, *Phys. Rev. B*, 2013, **88**, 174203.
17. V. L. Deringer, W. Zhang, P. Rausch, R. Mazzarello, R. Dronskowski and M. Wuttig, *J. Mater. Chem. C*, 2015, **3**, 9519-9523.
18. W. Zhang, I. Ronneberger, P. Zalden, M. Xu, M. Salinga, M. Wuttig and R. Mazzarello, *Sci Rep*, 2014, **4**, 6529.
19. W. Zhang, I. Ronneberger, Y. Li and R. Mazzarello, *Monatsh. Chem.*, 2014, **145**, 97-101.
20. Feng Rao, Keyuan Ding, Yuxing Zhou, Yonghui Zheng, Mengjiao Xia, Shilong Lv, Zhitang Song, Songlin Feng, Ider Ronneberger, Riccardo Mazzarello, Wei Zhang and E. Ma, *Science*, 2017, **358**, 1423-1426.
21. M. D. Ediger and P. Harrowell, *J Chem Phys*, 2012, **137**, 080901.
22. P. G. Debenedetti and F. H. Stillinger, *Nature*, 2001, **410**, 259-267.

23. T. Schenk, D. Holland-Moritz, V. Simonet, R. Bellissent and D. M. Herlach, *Phys. Rev. Lett.*, 2002, **89**, 075507.
24. G. Kresse and J. Hafner, *Phys. Rev. B*, 1993, **47**, 558-561.
25. G. Kresse and J. Furthmüller, *Comput. Mater. Sci.*, 1996, **6**, 15-50.
26. P. E. Blöchl, *Phys. Rev. B*, 1994, **50**, 17953-17979.
27. G. Kresse and D. Joubert, *Phys. Rev. B*, 1999, **59**, 1758-1775.
28. J. P. Perdew, K. Burke and M. Ernzerhof, *Phys. Rev. Lett.*, 1996, **77**, 3865-3868.
29. W. G. Hoover, *Phys. Rev. A*, 1985, **31**, 1695-1697.
30. S. Nosé, *J. Chem. Phys.*, 1984, **81**, 511-519.
31. M. Kuwahara, R. Endo, K. Tsutsumi, F. Morikasa, T. Tsuruoka, T. Fukaya, M. Suzuki, M. Susa, T. Endo and T. Tadokoro, *Jpn. J. Appl. Phys.*, 2013, **52**, 118001.
32. X. W. Fang, C. Z. Wang, Y. X. Yao, Z. J. Ding and K. M. Ho, *Phys. Rev. B*, 2010, **82**, 184204.
33. M. Werner, H. Mehrer and H. Siethoff, *J. Phys. C*, 1983, **16**, 6185-6195.
34. T. Satow, O. Uemura and Y. Sagara, *Phys. Status Solidi (a)*, 1982, **71**, 555-561.
35. V. L. Deringer, W. Zhang, M. Lumeij, S. Maintz, M. Wuttig, R. Mazzarello and R. Dronskowski, *Angew Chem Int Ed Engl*, 2014, **53**, 10817-10820.
36. W. Zhang, V. L. Deringer, R. Dronskowski, R. Mazzarello, E. Ma and M. Wuttig, *MRS Bull.*, 2015, **40**, 856-869.
37. M. Xu, Y. Q. Cheng, H. W. Sheng and E. Ma, *Phys Rev Lett*, 2009, **103**, 195502.
38. T. Matsunaga, J. Akola, S. Kohara, T. Honma, K. Kobayashi, E. Ikenaga, R. O. Jones, N. Yamada, M. Takata and R. Kojima, *Nat. Mater.*, 2011, **10**, 129-134.
39. Z. Sun, J. Zhou, A. Blomqvist, B. Johansson and R. Ahuja, *Appl. Phys. Lett.*, 2008, **93**, 061913.
40. B. E. Warren, B. L. Averbach and B. W. Roberts, *J. Appl. Phys.*, 1951, **22**, 1493-1496.
41. S. Le Roux and P. Jund, *Comput. Mater. Sci.*, 2010, **49**, 70-83.
42. J. Akola and R. O. Jones, *Phys. Rev. B*, 2007, **76**, 235201.
43. S. Caravati, M. Bernasconi, T. D. Kühne, M. Krack and M. Parrinello, *Appl. Phys. Lett.*, 2007, **91**, 171906.
44. J. Hegedus and S. R. Elliott, *Nat. Mater.*, 2008, **7**, 399-405.
45. S. Kohara, K. Kato, S. Kimura, H. Tanaka, T. Usuki, K. Suzuya, H. Tanaka, Y. Moritomo, T. Matsunaga, N. Yamada, Y. Tanaka, H. Suematsu and M. Takata, *Appl. Phys. Lett.*, 2006, **89**, 201910.